Nano Energy 92 (2022) 106700

Contents lists available at ScienceDirect

Nano Energy

journal homepage: www.elsevier.com/locate/nanoen

Anisotropic magnetic liquid metal film for wearable wireless electromagnetic sensing and smart electromagnetic interference shielding

Ruiqi Zhu [a,b], Zhenyang Li [a], Gao Deng [a], Yuanhang Yu [a], Jianglan Shui [a], Ronghai Yu [a], Caofeng Pan [b,*], Xiaofang Liu [a,*]

[a] School of Materials Science and Engineering, Beihang University, Beijing 100191, China
[b] CAS Ctr Excellence Nanosci, Beijing Key Lab Micronano Energy & Sensor, Beijing Inst Nanoenergy & Nanosyst, Beijing 101400, China

ARTICLE INFO

Keywords:
Magnetic liquid metal
Stretchable film
Electromagnetic interference shielding
Electromagnetic sensing

ABSTRACT

Smart and wearable electromagnetic (EM) functional materials that can reasonably use EM energy and prevent EM pollution are of great significance to the future information society, but their design and preparation are still challenging. Here, a multifunctional EM response film is prepared based on a magnetic liquid metal droplet-filled elastomer with magnetic field-induced anisotropic structure, which can reversibly construct conductive network and tune heterogeneous interface during cyclic stretching. This film can withstand up to 600% tensile strain and shows stretching-enhanced electrical conductivity. Its EM interference shielding effectiveness (SE) significantly increases with stretching, and the relative SE change ($\Delta SE/SE_0$) shows a linear response to the tensile strain. The specific shielding effectiveness (an ultrahigh value of 404 dB mm^{-1} at 400% strain) and strain sensitivity of the film outperform other stretchable EM functional materials. More interestingly, this film exhibits rapid switching between EM wave transmission and shielding through continuous stretching, which enables an off/on switchable EM interference shielding function. Furthermore, it can be used in a wearable EM sensor to wirelessly monitor human movements by recording changes of EM wave intensity.

1. Introduction

Electromagnetic (EM) wave is the cornerstone of the information and digital technology in modern society. It plays a role in transmitting signals, and also produces EM radiation pollution which interferes with the operation of electronic device and threatens human health [1–4]. Therefore, the development of EM functional materials that can reasonably utilize EM waves and prevent EM radiation has become a hot topic of practical significance [5–9]. Based on multiple EM response modes such as dipole polarization, charge transport and magnetic response [10–14], a variety of EM functional materials/devices have been designed and fabricated including EM interference (EMI) shielding materials, EM energy conversion materials, EM sensors, etc. [15–18]. Moreover, with the increasing demand for wearable and smart nano/micro-devices, a new generation of EM functional materials with excellent flexibility, high stretchability and high sensitivity to external stimuli has attracted considerable attention in recent years [19–22].

Smart EM interference (EMI) shielding materials and EM sensors are representative of state-of-the-art EM functional materials, which shield and utilize EM waves, respectively [23–26]. The key to their design and fabrication is the ultrathin, stretchable, performance-tunable and durable conductive films. Traditional EMI shielding films, composed of MXene, graphene, metal nanowires, etc., are not suitable for stretchable electronic devices due to their rapid performance degradation during bending and stretching. At the same time, their EM behaviors cannot be dynamically tuned via external stimuli. Fortunately, liquid metal (LM)-filled elastomer films with high electrical conductivity and superb deformability provide an effective solution. Yao et al. fabricated a LM network-filled polymer film (2 mm) and obtained strain-enhanced EMI shielding performance [27]. As the tensile strain increased to 400%, the shielding effectiveness increased twice (from 41.5 to 81.6 dB). Similarly, Yu et al. prepared a stretchable LM foam elastomer (3.6 mm), which could increase the shielding effectiveness from ~48–83 dB with the deformation of LM [28].

Despite these advances, there is still an urgent need to further significantly improve the EM response performances of LM-based EM films to realize new EM functions. For example, a LM-based film with a thinner thickness (e.g. <1 mm) and equivalent shielding effectiveness

* Corresponding authors.
E-mail addresses: cfpan@binn.cas.cn (C. Pan), liuxf05@buaa.edu.cn (X. Liu).

https://doi.org/10.1016/j.nanoen.2021.106700
Received 5 September 2021; Received in revised form 3 November 2021; Accepted 3 November 2021
Available online 11 November 2021

(>20 dB) will be attractive for the application in wearable electronic devices. A wider dynamic change range and a higher strain sensitivity of EMI shielding effectiveness may enable the LM-based film to realize off/on switching of shielding performance through continuous stretching, that is, a reversible conversion between EM wave transmission and shielding. This function has potential applications in smart EM protection and smart camouflage [29]. In addition, a LM-based film with linear response ability over a large dynamic range will be preferred for constructing EM sensor that is competitive in wireless and remote sensing [30–33]. Previous stretchable EM sensors are designed based on the change of resonant frequency of EM waves. If the EM sensor can be designed based on the change of EM signal intensity, it is expected to achieve a wider detection range and a higher sensitivity. However, the design and preparation of LM-based film with comprehensive advantages of higher EM response, wider dynamic change range, higher strain sensitivity and linear response ability remain huge challenges.

In this work, we developed a stretchable multifunctional EM response film based on a magnetic LM (MLM) droplet-filled Ecoflex elastomer with magnetic field-induced anisotropic structure (denoted as anisotropic magnetic liquid metal film, AMLM film). This AMLM film has excellent flexibility, stretchability (600%) strain-sensitive conductivity, and demonstrates new applications in smart EMI shielding and wireless EM sensor. Benefiting from the reversible construction of the MLM conductive network and the repeated expansion-contraction of the EM wave scattering interface, the EM properties of the film can be robustly regulated during cyclic stretching. The AMLM film shows strain-enhanced EMI shielding performance, and the relative SE change ($\Delta SE/SE_0$) increases linearly with the tensile strain. Compared with previously reported stretchable shielding materials, AMLM film has larger specific shielding effectiveness (SSE = 404 dB mm^{-1}), wider SE change range (up to ~16 times) and much higher strain sensitivity. These characteristics enable the AMLM film to realize an off/on switching of EMI shielding function. Furthermore, a wearable SE sensor model with a three-layer structure was designed based on the AMLM film, which can wirelessly monitor human movements according to the intensity change of EM signal.

2. Experimental section

2.1. Fabrication of AMLM and IMLM films

Pure liquid metal (LM) EGaln (mass ratio of Ga: 68.5 wt%, In: 21.5 wt %, Sn: 10 wt%, from Changsha Shengte New Material Co., Ltd.), Fe particles (1 μm, from Hefei AVIC Nano Technology Development Co., Ltd.) and polydimethylsiloxane (Ecoflex rubber, from Smooth-On Inc.) were used as raw materials. First, LM was added to the dilute hydrochloric acid ethanol solution (1.44 mol L^{-1}). After stirring for 5 min, Fe particles were added to the above suspension, and stirred until the Fe particles were completely mixed into LM to form MLM. The obtained MLM was washed several times with ethanol to remove residual HCl, and then dried under vacuum at room temperature overnight. Subsequently, MLM was mixed with Ecoflex rubber and stirred for 20 min using a glass rod. Finally, the mixture was cured under an external magnetic field for 4 h at room temperature. The obtained film contained large MLM droplets and were denoted as AMLM film. The Fe content in the films increased from 0.78 g (4 wt%), 1.0 g (5 wt%) to 1.2 g (6 wt%), and the contents of LM and Ecoflex rubber were fixed to 17.0 g and 2.0 g, respectively. To prepare isotropic magnetic liquid metal (IMLM) film, the mixture of MLM and Ecoflex rubber was cured for 4 h at room temperature without an external magnetic field. For AMLM film filled with small MLM droplets (denoted as AMLM-s film), MLM was mixed with Ecoflex rubber and stirred for 5 min using immersion shear disperser at a speed of 300 rpm.

2.2. Characterization

The crystal structure of the samples were characterized by X-ray diffractometer (XRD, D/MAX-2500) using Cu Kα radiation. Morphology, microstructure and elemental distribution were analyzed using a field emission scanning electron microscope (SEM, ZEISS Gemini 300) equipped with energy dispersive spectroscopy (EDS, OXFORD Xplore 30). Distribution of MLM and LM droplets in substrate was observed using an optical microscope. Mechanical properties of the samples were tested using a universal testing machine (Instron 5565, 5KN).

2.3. Measurement of EMI shielding performance

EMI shielding performances of the films under different tensile strains were tested by a vector network analyzer (N5234B PNA-L, KEYSIGHT) in the frequency range of 8.2–12.4 GHz. Before testing, a standard calibration process was performed. EMI shielding effectiveness is defined as the logarithmic ratio of incident power to transmission power. The total SE (SE_T) is the summary of reflection effectiveness (SE_R), absorption effectiveness (SE_A) and multiple reflection effectiveness (SE_M). SE_M can be ignored when SE_T is larger than 15 dB. Experimentally, scattering parameters (S_{11}, S_{21}, S_{21} and S_{22}) were measured and used to calculate SE_T, SE_A and SE_R according to the following equations.

$$SE_T = 10\log\left(\frac{1}{|S_{21}|^2}\right) \quad (1)$$

$$SE_R = 10\log\left(\frac{1}{1-|S_{11}|^2}\right)[f_0] \quad (2)$$

$$SE_A = 10\log\left(\frac{1-|S_{11}|^2}{|S_{21}|^2}\right)[f_0] \quad (3)$$

3. Results and discussion

3.1. Preparation of anisotropic magnetic liquid metal film

Fig. 1a illustrates the fabrication of AMLM film, which consists of gallium–indium–tin eutectic alloy, Fe particles and Ecoflex. First, the MLM was prepared by mixing Fe particles (1.0 g) into galinstan (17.0 g) with a low melting point (10.5 °C) and high conductivity (3.4×10^6 S m^{-1}). Due to the susceptibility to oxidation, galinstan and Fe particles are easily passivated by the oxide layers, which will restrict the diffusion and uniform dispersion of Fe particles in LM [34]. Therefore, the mixing of Fe particles and LM was conducted in a dilute hydrogen chloride solution under mechanical stirring. After stirring for 40 min, the black suspension became clear and transparent, indicating that the Fe particles were completely dispersed in the LM, and the obtained MLM can quickly respond to the external magnet (Figs. 1b and S1). Subsequently, the MLM and Ecoflex (2.0 g) were mechanically mixed and poured into a mold under a magnetic field. During this process, an oxide layer was formed on the surface of the LM to prevent Fe particles from detaching, thereby ensuring that the LM remained its magnetic property and was aligned along the direction of magnetic field (X direction). The size of MLM droplets in Ecoflex decreases as the mechanical stirring speed increases [14]. At the same stirring speed, the MLM droplets formed under external magnetic field are larger than those formed without external magnetic field (Fig. S2). Similarly, a series of AMLM films containing different amounts of LM and Fe were prepared. See the experimental section for details. The obtained AMLM film can be stretched, twisted and bent to a large extent (Figs. 1c and d), and can quickly recover its original shape without fracture and deformation.

The AMLM film composed of 5 wt% Fe and 10 wt% Ecoflex was selected as a representative sample for composition and microstructure

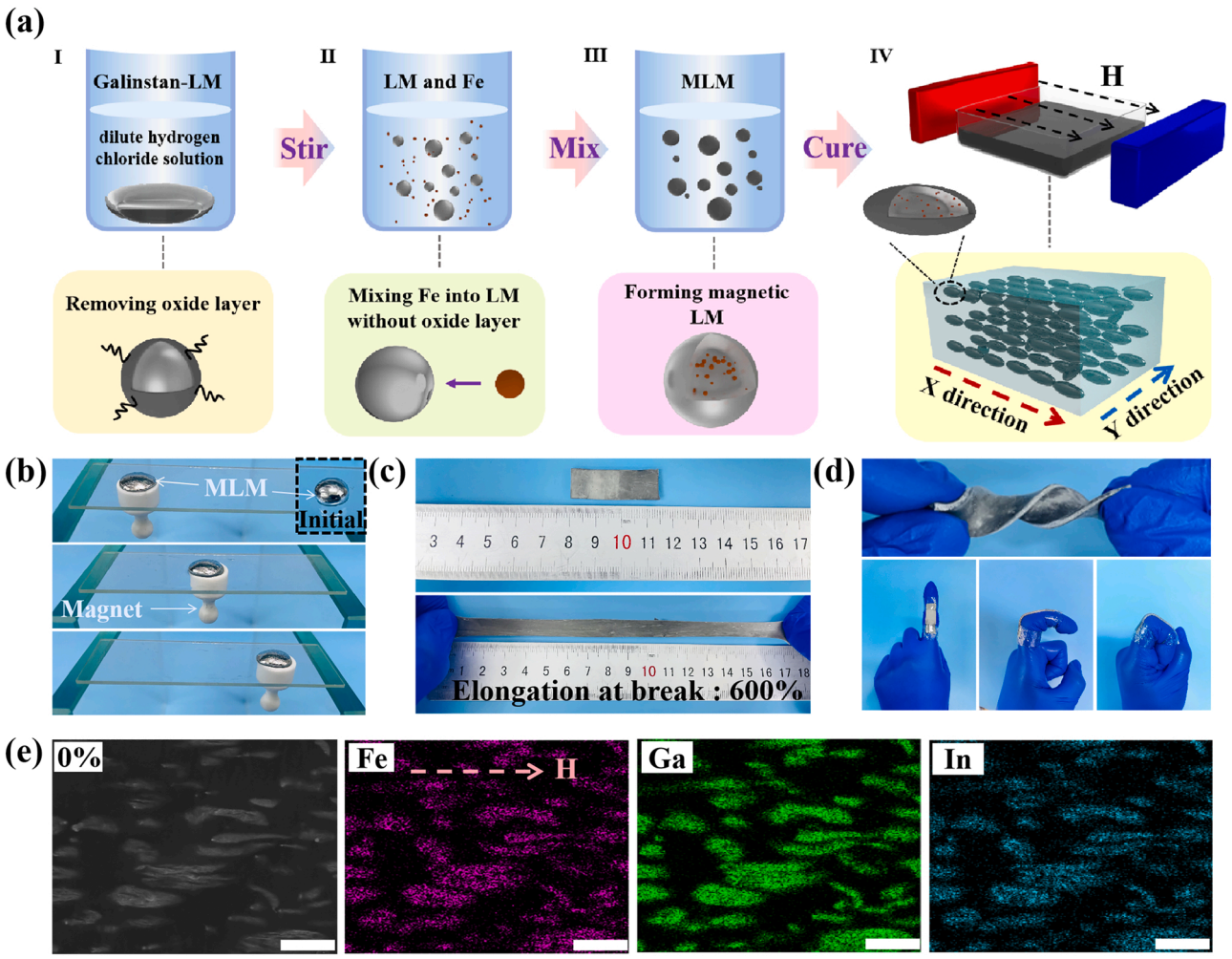

Fig. 1. Preparation and morphology of AMLM film. (a) Schematic illustration of the synthesis of AMLM film. (b) Photos showing the response of MLM to external magnet. (c, d) Photos showing stretching, twisting and bending AMLM film. (e) SEM image and EDS element mapping results of Fe, Ga and In in the AMLM film. Scale bars: 100 μm.

characterizations. Fig. S3 shows the XRD patterns of the MLM, pure Fe particles and pure LM. For MLM, the broad peak at 35° derives from amorphous galinstan. Expect for the diffraction peak of pure Fe at 45°, no diffraction peaks from Fe-based compound could be identified, indicating that the Fe particles are physically dispersed in the LM without alloying [34]. Thus, the obtained AMLM film shows ferromagnetism at room temperature (Fig. S4, Table S1). The SEM image of AMLM film in Fig. 1e demonstrates that the embedded MLM breaks into elongated droplets in the matrix during the mixing process. Further EDS mapping results reveal the uniform distribution of Ga, In and Fe components without any obvious agglomeration of Fe particles.

The size of MLM droplets is an important factor affecting the structure of the MLM film. We compared the microstructure of films filled with large and small MLM droplets. For the samples cured in the absence of an external magnetic field, both large and small MLM droplets are in quasi-spherical shape and randomly distribute in the Ecoflex substrates (Figs. 2a and S5a), forming isotropic MLM films (denoted as IMLM film and IMLM-s film, respectively). For the samples cured under an external magnetic field, the large MLM droplets are elongated and oriented along the direction of the magnetic field [35], showing an obvious anisotropic structure (Fig. 2b); however, the orientation and elongation of the small MLM droplets are relatively weak, which weakens the anisotropic characteristics of the corresponding AMLM-s film (Fig. S5b). Due to the excellent deformability of MLM and Ecoflex as well as the uniform dispersion of MLM, the AMLM film exhibits outstanding stretchability and can be stretched to ~600% strain (Fig. 1c). The changes of the microstructure of AMLM and IMLM films with strain were observed by optical microscope and SEM (Fig. 2a and b). When stretched in the magnetic-field direction (X direction), both oriented and unoriented MLM droplets become elongated and align along the X direction as strain increases. When the strain increases to 300%, the oriented MLM droplets form parallel rods of a few microns in length (parallel to the X direction). This structure change is essential for the film to significantly increase electrical conductivity under large stretching.

3.2. Anisotropic mechanical and conductive properties

The mechanical properties of the IMLM and AMLM films were further investigated using uniaxial tensile tests under ambient conditions. The stress-strain ($\sigma - \varepsilon$) curves were tested in different stretching directions (along the X and Y directions, Figs. 2c and S6), and the corresponding elastic modulus and elongation at break are compared in Fig. 2d and e. Both IMLM and AMLM films exhibit a remarkable increase in elongation at break and a significant decrease in elastic modulus in comparison with the pure Ecoflex film, which should be attributed to the good deformability of MLM. The improved flexibility and stretchability of the composite film make it suitable for stretchable EM functional materials. The orientation and elongation of the MLM droplets in the films endow the AMLM film with anisotropic mechanical properties. The AMLM film stretched in the X direction shows a higher elongation at

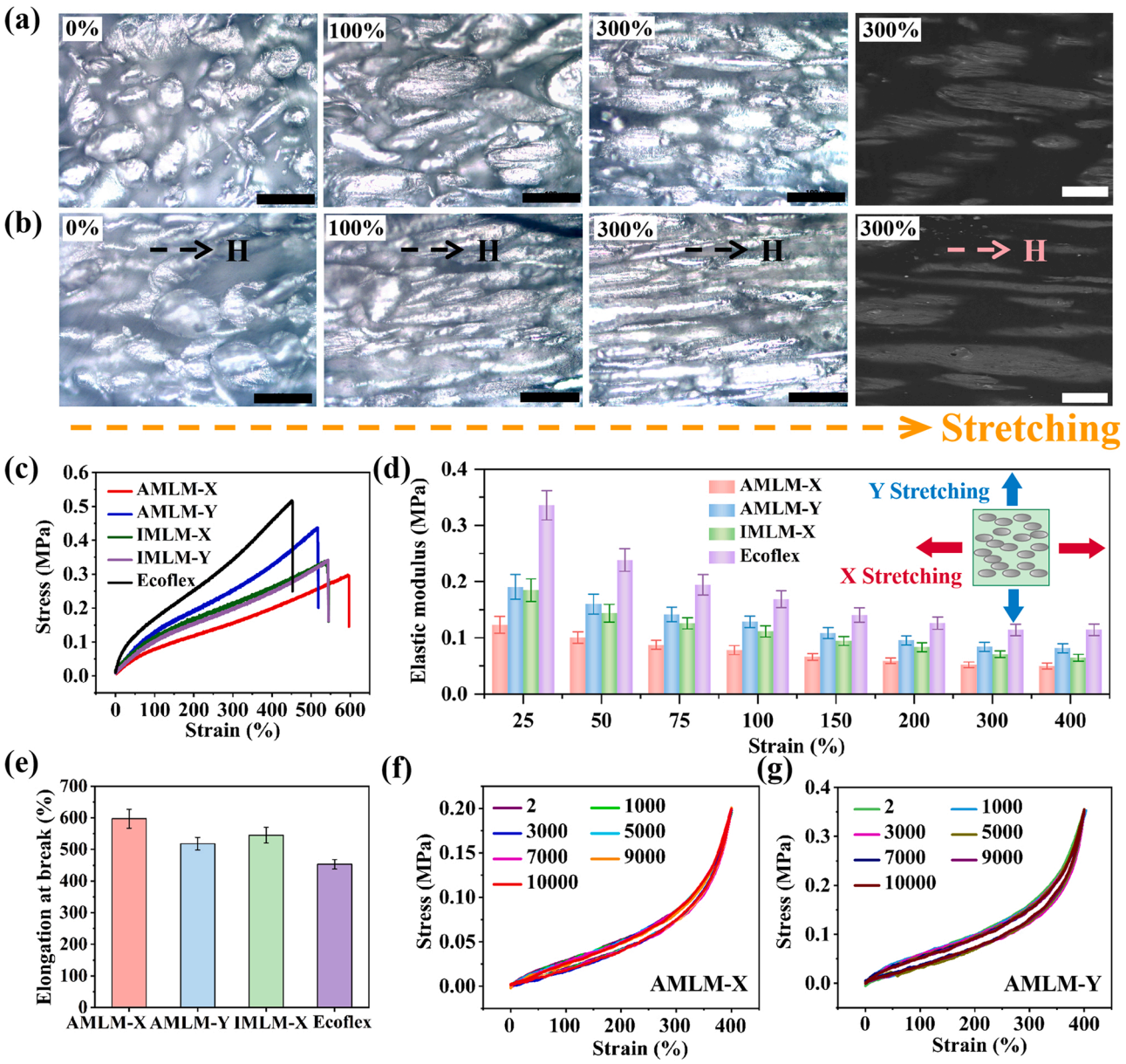

Fig. 2. Microstructure characteristics and mechanical properties. (a) Optical microscope images of IMLM film under 0%, 100%, 300% strains, and SEM image of IMLM film under 300% strain. Scale bars: 200 μm. (b) Optical microscope images of AMLM film under 0%, 100%, 300% strains, and SEM image of AMLM film under 300% strain. Scale bars: 200 μm. (c) Stress-strain curves of AMLM, IMLM and pure Ecoflex films. (d) Comparison of elongation at break of AMLM, IMLM and pure Ecoflex films. (e) Comparison of elastic modulus of AMLM, IMLM and pure Ecoflex films. (f, g) Cyclic stress-strain curves of AMLM film stretched along X and Y directions, respectively.

break of 600% and a lower elastic modulus of 0.049 MPa (at 400% strain) compared with the one stretched in the Y direction (518%, and 0.081 MPa at 400% strain). The IMLM film without anisotropic structure exhibits moderate elongation at break and elastic modulus in both X and Y directions. It should be noted that droplet size affect the anisotropy of the mechanical properties. The smaller the droplets, the weaker the anisotropy of the AMLM film (Fig. S7). In addition, we tested the cyclic $\sigma - \varepsilon$ curves of the AMLM film under a constant strain of 400% (Fig. 2f and g), showing an apparent Mullins effect [36,37]. The AMLM film exhibits stable mechanical properties during 10,000 stretching cycles, which is beneficial to improving the service life of the devices. The strain decreases to zero as the stress is released, indicating the complete shape recovery without plastic deformation.

To visually reflect the change of electrical conductivities (σ_e) of the AMLM film during stretching, the film was connected into a circuit to power a LED (Fig. 3a). As the tensile strain increases, the LED becomes brighter and brighter, demonstrating a gradual increase in conductivity. We further measured the σ_e values of the IMLM and AMLM films under different strains and used COMSOL Multiphysics software to conduct finite element simulation for analysis. When stretched in the X direction, the conductivity measured in the X and Y directions are denoted as $\sigma_{e(XX)}$ and $\sigma_{e(XY)}$, respectively. Similarly, when stretched in the Y direction, $\sigma_{e(YX)}$ and $\sigma_{e(YY)}$ correspond to the conductivity measured in the X and Y directions, respectively. As shown in Figs. 3b and S8, all these films have low conductivities in the unstretched state, and show a sharp increase in conductivity as strain increases. The increase in conductivity by stretching can be attributed to two reasons. On the one hand, the MLM droplets with excellent deformability gradually elongate during stretching. Due to the constant volume (the Poisson's ratio of ~0.5), the MLM films will be compressed in the Y (perpendicular to the magnetic-

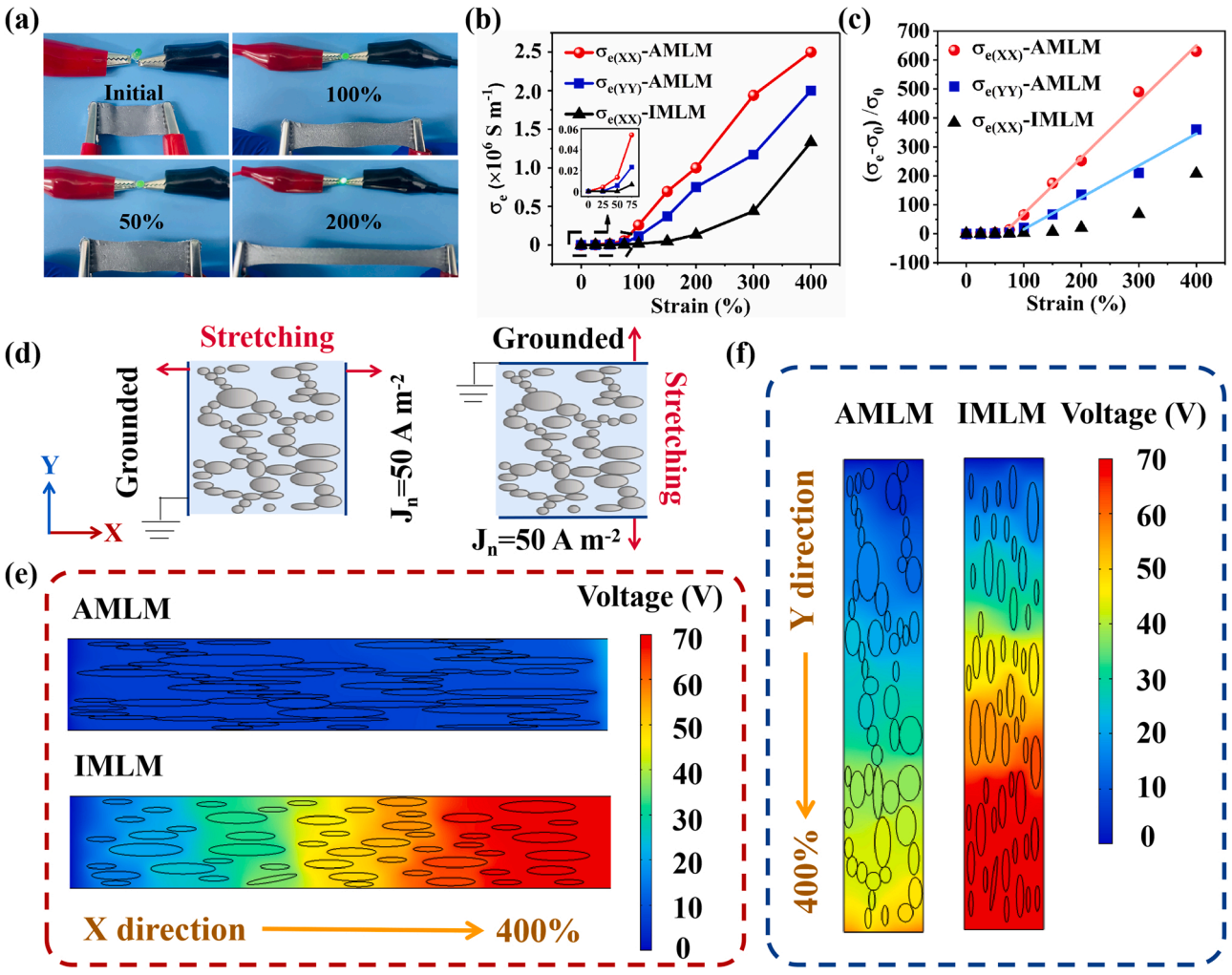

Fig. 3. Change of conductivity with tensile strain. (a) Photos showing the change of brightness of LED during stretching. (b) Conductivity versus tensile strain curves of AMLM and IMLM films. (c) Relative conductivity change versus tensile strain curves of AMLM and IMLM films. (d) 2D models of AMLM film used for simulation. Stretching direction is parallel to electrical current direction. (e) Simulation results of X-directional electrical potential distribution of AMLM and IMLM films stretched in the X direction. (f) Simulation results of Y-directional electrical potential distribution of the AMLM and IMLM films stretched in the Y direction.

field direction) and Z (thickness direction) directions, leading to a sharp reduction in the distance between the elongated MLM droplets and even direct contact between them [38]. On the other hand, as simulated in Fig. S9, the electrical current concentrates at the tips of the elongated MLM droplets and enhances the conductivity of the adjacent substrate [27]. Therefore, as the strain increases, the elongation and vertical-distance reduction of the MLM droplets can significantly increase the conductive paths and enhance the conductivity of adjacent substrate, leading to a significant increase in the total conductivity of the composite film.

Under the same strain, the conductivity of the three films follows the sequence: X-direction stretched AMLM > Y-direction stretched AMLM> X-direction stretched IMLM. We conducted finite element simulations to verify this order of conductivity, and built the 2D models based on the microstructure obtained from SEM images. The deformation of LM and substrate was set according to their Poisson's ratio [39]. In the simulation, one side of the 2D model is grounded, and the current density through the other side is constant at 50 A m^{-2} (Figs. 3d and S10). Fig. 3e–f and Fig. S11–12 show the simulation results of the electrical potential distribution of AMLM and IMLM films under 400% strain when stretched in the X and Y directions, respectively. When the color changes from blue to red, the electrical potential increases monotonically, and a larger color gradient suggests a higher resistance of the film. It is clear that the color gradient of the stretched AMLM film is smaller than that of the stretched IMLM film, indicating the lower resistivity of the AMLM film, which is consistent with the experimental results. The above comparison demonstrates the superiority of AMLM film in achieving ultrahigh electrical conductivity, which is desirable for stretchable high-performance EMI shielding materials.

The sensitivity of conductivity to strain was further evaluated by calculating the relative conductivity change $\Delta\sigma_e/\sigma_{e0} = (\sigma_e - \sigma_{e0})/\sigma_{e0}$ (Figs. 3c and S13). Under the same strain, the relative conductivity change of the AMLM film is much larger than that of the IMLM film, indicating that the anisotropic structure is beneficial to improve the response sensitivity of the film. Especially, the $\Delta\sigma_{e(xx)}/\sigma_{e0(xx)}$ and $\Delta\sigma_{e(YY)}/\sigma_{e0(YY)}$ of the AMLM film presents a linear relationship with strain (after 75% strain). When the strain increases to 400%, the conductivity of the AMLM film stretched in the X and Y directions increases by three orders of magnitude. The conductivity increment of the AMLM film is much larger than that of the previously reported LM-filled elastomers, where LM formed a continuous 3D network and stretching only caused a several-fold increment of conductivity. The high sensitivity of conductivity to strain endows the AMLM film with bright applications as EM sensors and switchable EMI shielding materials.

3.3. Strain-sensitive electromagnetic interference shielding performance

The excellent stretchability and strain-sensitive conductivity make

AMLM film an ideal candidate for switchable EMI shielding materials. The scattering parameters (S_{11}, S_{12}, S_{21} and S_{22}) of the AMLM and IMLM films with thickness of ~0.8 mm were tested in 8.2–12.4 GHz using a vector network analyzer. The propagation direction of EM wave is perpendicular to the film, and the electric field direction of the EM wave is parallel to the Y direction (Fig. 4a). Fig. 4b shows the EMI shielding performance of AMLM film as a function of X-directional tensile strain. The total shielding effectiveness (SE_{TX}) of the unstretched AMLM film is 20.6 dB. When stretched in the X direction, its SE_{TX} monotonously increases, and reaches a remarkable value of 80.7 dB at 400% strain. If the electric field direction of the EM wave is parallel to the X direction and the stretching direction is parallel to the Y direction, the obtained SE_{TY} increases from 17.7 to 68.6 dB (Fig. S14). For IMLM film, its SE_{TX} and SE_{TY} values are similar, and lower than those of AMLM film (Figs. 4c and S15).

Considering the decrease of film thickness during stretching, the specific SE_T value (SSE_T =SE_T/thickness) of the films were calculated to more clearly reflect the EMI shielding ability (Fig. 4d) [40,41]. The AMLM film exhibits ultrahigh SSE_{TX} of ~404 dB mm^{-1} and SSE_{TY} of ~343 dB mm^{-1} under 400% strain. Under the same strain, the SSE_T values of AMLM film are much higher than those of IMLM film. In comparison with previously reported stretchable EMI shielding materials (Fig. 4f, Table S2), the SSE_T values of AMLM film are ranked at the top [27,28,42–52]. Moreover, when the strain increases to 400%, the change of SSE_T value of AMLM film is more than 1500%, higher than the 1031% increase of the SSE_T of the IMLM film. The above comparison highlights the superiority of anisotropic structure of MLM in improving EMI shielding ability and strain sensitivity.

Since the total shielding efficiency includes the contributions from absorption (SE_A), reflection (SE_R) and multiple reflections (negligible for SE_T > 15 dB). The average SE_{AX} and SE_{RX} of AMLM film were calculated to analyze the EMI shielding mechanism (Fig. 4e). As the strain increases

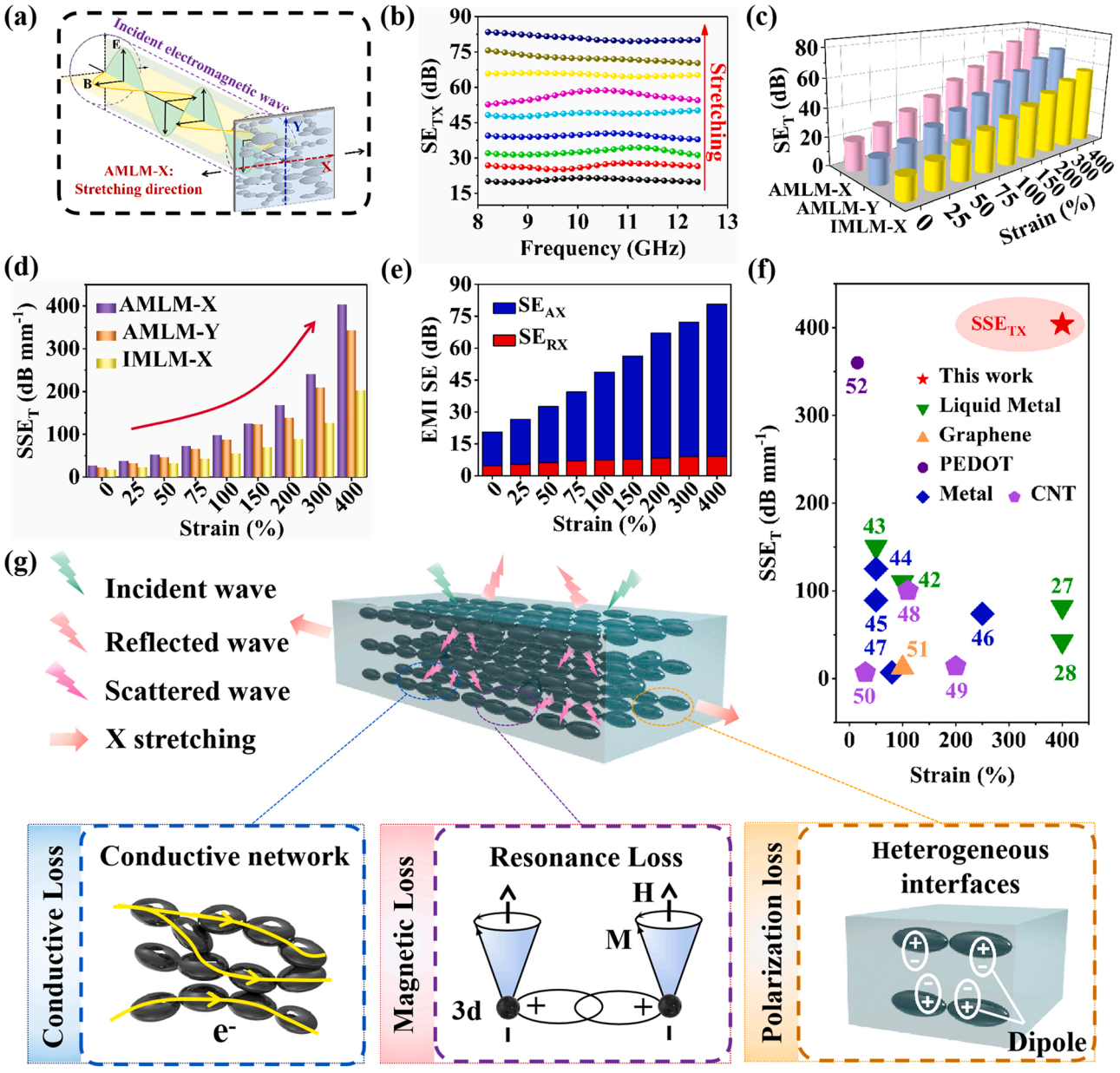

Fig. 4. EMI shielding performances and related mechanisms. (a) Schematic illustration of measuring the scattering parameters of the film. (b) SE_{TX} of AMLM film under different tensile strains of 0%, 25%, 50%, 75%, 100%, 150%, 200%, 300% and 400%. (c) Comparison of SE_{AX} and SE_{RX} of AMLM film under different tensile strains. (d) Comparison of SSE_T of AMLM and IMLM films under different tensile strains. (e) SE_{AX} and SE_{RX} of AMLM and IMLM films under different tensile strains. (f) Comparison of SSE_T of AMLM and other stretchable EMI shielding materials. (g) Schematic illustration of reflection and absorption of EM waves by AMLM film.

from 0% to 400%, SE_{RX} slightly increases from 5.3 to 9.1 dB, while SE_{AX} sharply increases from 21.3 to 71.7 dB, indicating the dominant contribution of SE_{AX} to SE_{TX}. Similar conclusions can be obtained by calculating SE_{AY} and SE_{RY} (Fig. S14c). The increase of SE_T with tensile strain for AMLM film can be explained in terms of the unique characteristics of MLM. For highly conductive materials, conductivity is the most critical factor in determining shielding performance, and SE_R and SE_A can be approximately expressed as [53,54]:

$$SE_R = \log\left(\frac{\sqrt{\mu_0\sigma}}{4\sqrt{2\pi f\mu\varepsilon_0}}\right) \quad (4)$$

$$SE_A = 8.68d\sqrt{\pi f\mu\sigma} \quad (5)$$

where f is the frequency, μ is the permeability of the material, μ_0 and ε_0 are the permeability and permittivity of free space, and d is the thickness of the material. Figs. S16–S18 and Table S3 show the power coefficients of absorption, reflection and transmission of the films, as well as the permittivity and permeability. The increase in EM wave reflection is mainly due to the increase in conductivity, while the increase in EM wave absorption derives from several reasons. Firstly, as the conductivity increases, more EM energy can be converted into thermal energy through the enhanced induced current under alternating

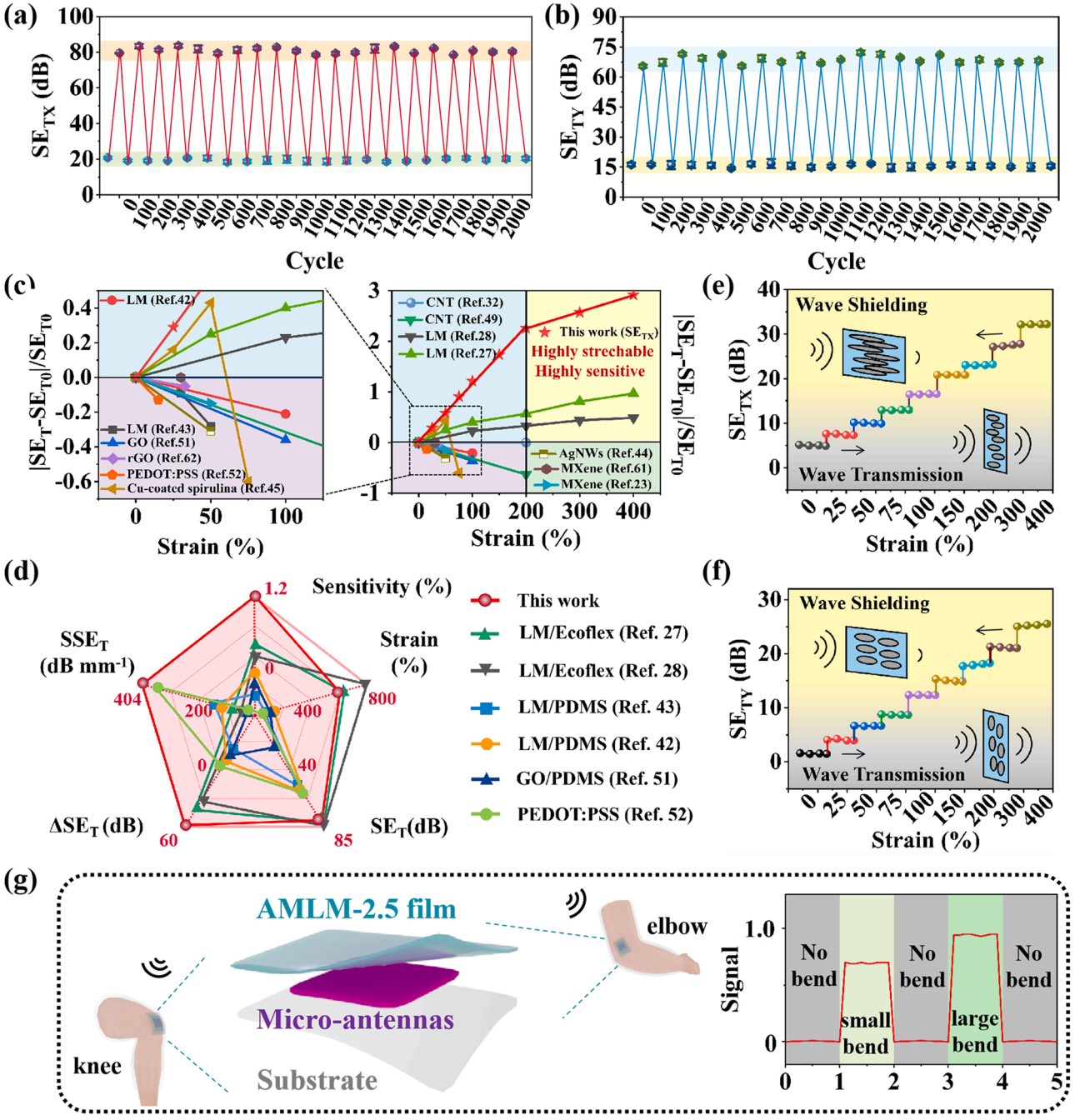

Fig. 5. EM response characteristics of smart EMI shielding material and wireless EM sensor. (a, b) SE_{TX} and SE_{TY} of AMLM film under cyclic stretching. (c) Comparison of strain sensitivity between AMLM film ($\Delta SE_{TX}/SE_{T0}$) and other stretchable shielding materials. (d) A radar plot showing a comparison among stretchable shielding materials. (e, f) Variations of SE_{TX} and SE_{TY} of AMLM-2.5 film with tensile strain, showing off/on switchable EMI shielding function. (g) Scheme of flexible EM sensor integrated with AMLM film, micro-antennas and biocompatible substrate. Signal = SE_T/SE_{T0}.

EM field. Secondly, the increase in permeability during stretching, possibly caused by the enhanced magnetic anisotropy, enhances the magnetic resonant loss [55–57]. In addition, MLM droplets elongate with increasing strain, creating more heterogeneous interfaces between LM and Ecoflex. Hence, the interfacial polarization loss deriving from the accumulation of free charges is enhanced, which plays a secondary role in improving EM wave absorption [58–60]. Moreover, the probability of multiple scattering of EM waves at the interfaces is considerably enhanced, which increases the transmission path of EM waves and thus promotes the attenuation of EM waves. Fig. 4g summarizes the EMI shielding mechanism of the AMLM film.

The anisotropic structure of AMLM film is closely related to the magnetic response of MLM droplets under the magnetic field, which depends on the size of MLM droplets and the content of Fe particles. Due to the weaker anisotropic structure of the AMLM-s film filled with small MLM droplets, its conductivity, SE_T and the strain sensitivity are lower than the AMLM film filled with large MLM droplets (Fig. S19). In addition, we prepared two control films containing fewer (4 wt%) and more (6 wt%) Fe particles. The reduction of Fe content weakens the anisotropy and magnetic permeability of the AMLM film (Fig. S20 and Table S4), while the increase of Fe content decreases the conductivity of the AMLM film (Fig. S21), all of which can reduce the reflection and absorption of EM waves. An optimal Fe content of 5 wt% is determined for the best EMI shielding performance when stretched in both X and Y directions (Fig. S22).

3.4. Smart electromagnetic interference shielding and wireless EM sensing

For AMLM film, the significant change of shielding effectiveness with strain indicates its potential applications in switchable EMI shielding and EM sensing. However, in practical applications, shielding effectiveness is also required to have high cycle stability and high strain sensitivity. Here, we measured the cycle stability of the SE_T values of the AMLM film by repeatedly stretching and releasing the film. As shown in Figs. 5a–b and S23, the conversion between strong shielding (400% strain) and weak shielding (0% strain) is reversible, and the SE_{TX} and SE_{TY} values are durable and show negligible decay after 2000 stretch-release cycles. The strain sensitivity of shielding effectiveness is defined as $\Delta SE_T/SE_{T0} = (SE_T - SE_{T0})/SE_{T0}$, where SE_{T0} and SE_T are the total shielding effectiveness without and with tensile strain, respectively. As shown in Fig. 5c, the relative SE_T change of AMLM film shows linear response to the strain in the strain range of 0–200% and 200–400%, respectively. The EMI shielding performance of the AMLM film is superior to the previously reported stretchable EMI shielding materials, which were filled with liquid metal, MXene, CNTs, graphene, Ag nanowires, copper-coated spirulina and PEDOT [23,27,28,32,42–45,49,51,52,61,62]. For stretchable shielding materials filled with rigid solid fillers, the SE_T decreases with tensile strain, which is not suitable for integration with stretchable and wearable electronic devices. Although 3D LM-filled materials exhibits strain-enhanced shielding performance, the strain sensitivity is much lower than that of AMLM film. This is because the initial conductivity of the continuous 3D LM network is very high, which endows the unstretched materials with high SE_{T0} values, leading to the low sensitivity. In contrast, MLM droplets are separated in Ecoflex, and rapidly elongated and oriented under stretching, which leads to the significant increase of conductivity and SE_T value. A radar plot is presented in Fig. 5d to evaluate the comprehensive performances of AMLM film. Obviously, our AMLM film shows superiority in stretchability, SE_T, ΔSE_T, SSE_T and strain sensitivity.

The excellent cycling stability and strain-sensitivity of AMLM film allows us to conceive new EM functional materials. For example, if the content of MLM droplets in Ecoflex is reduced to 2.5 wt% (denoted as AMLM-2.5 film), an off/on switchable smart EMI shielding film can be obtained. As shown in Figs. 5e–f and S24, the SE_{TX} and SE_{TY} of the unstretched AMLM-2.5 film are as low as ~4.8 and 1.6 dB, respectively, allowing most of the incident EM waves to penetrate the film, which corresponds to the “off-state”. The increase in tensile strain causes a linear increase of relative SE_{TX} and SE_{TY} changes (Fig. S25). As the strain reaches 400%, SE_{TX} and SE_{TY} increase to ~32.2 and 25.2 dB, respectively, meeting the commercial application requirement of 20 dB, which is regarded as the "on state" of the shielding function. Cyclic testing shows excellent reversible and durable conversion between the off and on states of the EMI shielding (Fig. S26). This off/on switchable EMI shielding film has potential applications in sophisticated and high-precision EM protection systems as well as active camouflage systems [29].

Furthermore, this AMLM-2.5 film can be assembled into a wearable strain sensor to wirelessly monitor human biologic activities. We designed a three-layer device consisting of an upper layer of AMLM film-2.5, a middle layer of flexible micro-antennas and a lower layer of biocompatible substrate (Fig. 5g). The remote EM wave is used as a detection signal, which is received by the micro-antenna and further wirelessly transmitted to the signal monitoring device. When the elbow (or knee for example) is straightened, the SE_T of the unstretched AMLM-2.5 film is quite low, allowing most of the incident EM waves to pass through, and the detection signal will be displayed on the detection instrument. Once the AMLM-2.5 film is stretched due to the bending of the elbow (or knee), the SE_T of the stretched film increases. Thus, the transmission of EM waves will be blocked, and the detection instrument will display weak signal or no signal. Using this EM sensor, we will know the bending number, frequency and degree of elbow/knee, realizing dynamically recording the movement of the human body. Different from previous sensors based on resistance changes [63–67], we have designed a new sensor using electromagnetic wave signals.

4. Conclusion

In summary, we have prepared a multifunctional EM response film by filling magnetic liquid metal droplets into Ecoflex substrate under an external magnetic field. This flexible and stretchable film shows linear increase of relative conductivity ($\Delta\sigma/\sigma_0$) and relative SE_T ($\Delta SE_T/SE_{T0}$) with strain when being applied a uniaxial tensile stress. Benefitting from the anisotropic structure, the AMLM film has an ultrahigh SSE_T value that outperforms other stretchable EMI shielding materials, and its strain sensitivity of SE_T is also the highest among stretchable EMI shielding materials. An off/on switchable EMI shielding function is achieved by stretching the AMLM film, i.e. a reversible conversion between EM wave transmission and shielding. In addition, a wearable EM sensor is proposed, which has the potential to wirelessly detect the movement of human body using EM waves as signals. This work provides new materials and design ideas for wearable and smart EM functional materials.

CRediT authorship contribution statement

Ruiqi Zhu: Performing the experiments, Methodology, Data curation, Software, Formal analysis, Writing – original draft, Conducting the finite element simulation. **Zhenyang Li:** Analyzing results, Validation, Formal analysis. **Gao Deng:** Testing, Investigation. **Yuanhang Yu:** Methodology. **Jianglan Shui:** Writing – review & editing. **Ronghai Yu:** Resources, Supervision, Formal analysis, Funding acquisition. **Caofeng Pan:** Writing – review & editing, Supervision. **Xiaofang Liu:** Project administration, Writing – review & editing, Resources, Supervision, Validation, Funding acquisition.

Declaration of Competing Interest

The authors declare that they have no known competing financial interests or personal relationships that could have appeared to influence the work reported in this paper.

Acknowledgements

This work was financially supported by the National Natural Science Foundation of China (51971008, U1832138, 51731002, 51671010, 52125205 and U20A20166), Beijing Natural Science Foundation (2212033, Z180011), Science and Technology on Optical Radiation Laboratory Foundation (61424080412) and the Fundamental Research Funds for the Central Universities. We thank Wenbin Xu, Xin Sun and Junzhe He for their help in testing electromagnetic parameters.

Appendix A. Supporting information

Supplementary data associated with this article can be found in the online version at doi:10.1016/j.nanoen.2021.106700.

References

[1] T. Kim, G. Kim, H. Kim, H.J. Yoon, T. Kim, Y. Jun, T.H. Shin, S. Kang, J. Cheon, D. Hwang, B.W. Min, W. Shim, Nat. Commun. 10 (2019) 653.
[2] A. Iqbal, F. Shahzad, K. Hantanasirisakul, M.K. Kim, J. Kwon, J. Hong, H. Kim, D. Kim, Y. Gogotsi, C.M. Koo, Science 369 (2020) 446–450.
[3] J. Zeng, X. Ji, Y. Ma, Z. Zhang, S. Wang, Z. Ren, C. Zhi, J. Yu, Adv. Mater. 30 (2018), 1705380.
[4] Z. Song, X. Liu, X. Sun, Y. Li, X. Nie, W. Tang, R. Yu, J. Shui, Carbon 151 (2019) 36–45.
[5] Q. Song, F. Ye, X. Yin, W. Li, H. Li, Y. Liu, K. Li, K. Xie, X. Li, Q. Fu, L. Cheng, L. Zhang, B. Wei, Adv. Mater. 29 (2017), 1701583.
[6] Q. Wei, S. Pei, X. Qian, H. Liu, Z. Liu, W. Zhang, T. Zhou, Z. Zhang, X. Zhang, H. M. Cheng, W. Ren, Adv. Mater. 32 (2020), 1907411.
[7] Z. Ma, S. Kang, J. Ma, L. Shao, Y. Zhang, C. Liu, A. Wei, X. Xiang, L. Wei, J. Gu, ACS Nano 14 (2020) 8368–8382.
[8] J. Wang, L. Liu, S. Jiao, K. Ma, J. Lv, J. Yang, Adv. Funct. Mater. 30 (2020), 2002595.
[9] J. Zhang, N. Kong, S. Uzun, A. Levitt, S. Seyedin, P.A. Lynch, S. Qin, M. Han, W. Yang, J. Liu, X. Wang, Y. Gogotsi, J.M. Razal, Adv. Mater. 32 (2020), 2001093.
[10] Y. Li, X. Liu, X. Nie, W. Yang, Y. Wang, R. Yu, J. Shui, Adv. Funct. Mater. 29 (2019), 1807624.
[11] Z. Song, X. Sun, Y. Li, W. Tang, G. Liu, J. Shui, X. Liu, R. Yu, ACS Appl. Mater. Interfaces 13 (2021) 5266–5274.
[12] X. Sun, Y. Pu, F. Wu, J. He, G. Deng, Z. Song, X. Liu, J. Shui, R. Yu, Chem. Eng. J. 423 (2021), 130132.
[13] P. Li, Z. Lu, Small Sci. 1 (2020), 2000015.
[14] M.J. Ford, D.K. Patel, C. Pan, S. Bergbreiter, C. Majidi, Adv. Mater. 32 (2020), 2002929.
[15] F. Shahzad, M. Alhabeb, C.B. Hatter, B. Anasori, B.H. Hong, C.M. Koo, Y. Gogotsi, Science 353 (2016) 1137–1140.
[16] Q. Zhang, Q. Liang, Z. Zhang, Z. Kang, Q. Liao, Y. Ding, M. Ma, F. Gao, X. Zhao, Y. Zhang, Adv. Funct. Mater. 28 (2018), 1703801.
[17] M. Cao, X. Wang, W. Cao, X. Fang, B. Wen, J. Yuan, Small (2018), e1800987.
[18] Z. Zeng, H. Jin, M. Chen, W. Li, L. Zhou, Z. Zhang, Adv. Funct. Mater. 26 (2016) 303–310.
[19] H. Lv, Z. Yang, S.J.H. Ong, C. Wei, H. Liao, S. Xi, Y. Du, G. Ji, Z.J. Xu, Adv. Funct. Mater. 29 (2019), 1900163.
[20] Y. Yang, S. Chen, W. Li, P. Li, J. Ma, B. Li, X. Zhao, Z. Ju, H. Chang, L. Xiao, H. Xu, Y. Liu, , ACS Nano 14 (2020) 8754–8765.
[21] S. Wang, D. Li, Y. Zhou, L. Jiang, ACS Nano 14 (2020) 8634–8645.
[22] Q. Liu, X. Liu, H. Feng, H. Shui, R. Yu, Chem. Eng. J. 314 (2017) 320–327.
[23] W. Chen, L.X. Liu, H.B. Zhang, Z.Z. Yu, ACS Nano 15 (2021) 7668–7681.
[24] J. Xu, R. Li, S. Ji, B. Zhao, T. Cui, X. Tan, G. Gou, J. Jian, H. Xu, Y. Qiao, Y. Yang, S. Zhang, T.L. Ren, ACS Nano 15 (2021) 8907–8918.
[25] Y. Zhu, J. Liu, T. Guo, J.J. Wang, X. Tang, V. Nicolosi, ACS Nano 15 (2021) 1465–1474.
[26] Q. Liu, Q. Cao, H. Bi, C. Liang, K. Yuan, W. She, Y. Yang, R. Che, Adv. Mater. 28 (2016) 486–490.
[27] B. Yao, W. Hong, T. Chen, Z. Han, X. Xu, R. Hu, J. Hao, C. Li, H. Li, S.E. Perini, M. T. Lanagan, S. Zhang, Q. Wang, H. Wang, Adv. Mater. 32 (2020), 1907499.
[28] D. Yu, Y. Liao, Y. Song, S. Wang, H. Wan, Y. Zeng, T. Yin, W. Yang, Z. He, Adv. Sci. 7 (2020), 2000177.
[29] X. Liu, Y. Li, X. Sun, W. Tang, G. Deng, Y. Liu, Z. Song, Y. Yu, R. Yu, L. Dai, J. Shui, Matter 4 (2021) 1735–1747.
[30] M.S. Cao, X.X. Wang, M. Zhang, W.Q. Cao, X.Y. Fang, J. Yuan, Adv. Mater. 32 (2020), 1907156.
[31] W. Cao, C. Ma, S. Tan, M. Ma, P. Wan, F. Chen, Nano Micro Lett. 11 (2019) 72.
[32] Y. Li, X. Tian, S.P. Gao, L. Jing, K. Li, H. Yang, F. Fu, J.Y. Lee, Y.X. Guo, J. Ho, P. Y. Chen, Adv. Funct. Mater. 30 (2019), 1907451.
[33] W. Tang, X. Liu, Y. Li, Y. Pu, Y. Lu, Z. Song, Q. Wang, R. Yu, J. Shui, Nano Res. 13 (2020) 447–454.
[34] L. Ren, S. Sun, G. Casillas-Garcia, M. Nancarrow, G. Peleckis, M. Turdy, K. Du, X. Xu, W. Li, L. Jiang, S.X. Dou, Y. Du, Adv. Mater. 30 (2018), 1802595.
[35] B. Ma, C. Xu, J. Chi, J. Chen, C. Zhao, H. Liu, Adv. Funct. Mater. 29 (2019), 1901370.
[36] G. Machado, G. Chagnon, D. Favier, Mech. Mater. 42 (2010) 841–851.
[37] S. Wang, S.A. Chester, Int. J. Solids Struct. 136–137 (2018) 125–136.
[38] S.Y.T.G. Yun, S. Sun, D. Yuan, Q. Zhao, L. Deng, S. Yan, H. Du, M.D. Dickey, W. Li, Nat. Commun. 10 (2019) 1300.
[39] G. Yun, S.Y. Tang, Q. Zhao, Y. Zhang, H. Lu, D. Yuan, S. Sun, L. Deng, M.D. Dickey, W. Li, Matter 3 (2020) 824–841.
[40] C. Wang, Y. Gong, B.V. Cunning, S. Lee, Q. Le, S.R. Joshi, O. Buyukcakir, H. Zhang, W.K. Seong, M. Huang, M. Wang, J. Lee, G.H. Kim, R.S. Ruoff, Sci. Adv. 7 (2021), eabe3767.
[41] Z. Zeng, F. Jiang, Y. Yue, D. Han, L. Lin, S. Zhao, Y.B. Zhao, Z. Pan, C. Li, G. Nystrom, J. Wang, Adv. Mater. 32 (2020), 1908496.
[42] M. Zhang, P. Zhang, Q. Wang, L. Li, S. Dong, J. Liu, W. Rao, J. Mater. Chem. C 7 (2019) 10331–10337.
[43] L.C. Jia, X.X. Jia, W.J. Sun, Y.P. Zhang, L. Xu, D.X. Yan, H.J. Su, Z.M. Li, ACS Appl. Mater. Interfaces 12 (2020) 53230–53238.
[44] J. Jung, H. Lee, I. Ha, H. Cho, K.K. Kim, J. Kwon, P. Won, S. Hong, S.H. Ko, ACS Appl. Mater. Interfaces 9 (2017) 44609–44616.
[45] C. Liu, J. Cai, P. Dang, X. Li, D. Zhang, ACS Appl. Mater. Interfaces 12 (2020) 12101–12108.
[46] P.D. Feng, Z.H. Ye, Q.Y. Wang, Z. Chen, G.T. Wang, X.L. Liu, K. Li, W.W. Zhao, J. Mater. Sci. 55 (2020) 8576–8590.
[47] X. Hu, L. Mou, Z. Liu, Chin. Phys. B 30 (2021), 018401.
[48] Y. Kato, M. Horibe, S. Ata, T. Yamada, K. Hata, RSC Adv. 7 (2017) 10841–10847.
[49] D. Feng, D. Xu, Q. Wang, P. Liu, J. Mater. Chem. C 7 (2019) 7938–7946.
[50] K. Huang, M. Chen, G. He, X. Hu, W. He, X. Zhou, Y. Huang, Z. Liu, Carbon 157 (2020) 466–477.
[51] Z. Wang, W. Yang, R. Liu, X. Zhang, H. Nie, Y. Liu, Compos. Sci. Technol. 206 (2021) 0266–3538.
[52] P. Li, D. Du, L. Guo, Y. Guo, J. Ouyang, J. Mater. Chem. C 4 (2016) 6525–6532.
[53] Y.J. Wan, X.Y. Wang, X.M. Li, S.Y. Liao, Z.Q. Lin, Y.G. Hu, T. Zhao, X.L. Zeng, C. H. Li, S.H. Yu, P.L. Zhu, R. Sun, C.P. Wong, ACS Nano 14 (2020) 14134–14145.
[54] W.L. Song, M.S. Cao, M.M. Lu, S. Bi, C.Y. Wang, J. Liu, J. Yuan, L.Z. Fan, Carbon 66 (2014) 67–76.
[55] D. Lan, M. Qin, R. Yang, S. Chen, H. Wu, Y. Fan, Q. Fu, F. Zhang, J. Colloid Interface Sci. 533 (2019) 481–491.
[56] H. Wu, J. Liu, H. Liang, D. Zang, Chem. Eng. J. 393 (2020), 124743.
[57] W. Liu, L. Liu, G. Ji, D. Li, Y. Zhang, J. Ma, Y. Du, ACS Sustain. Chem. Eng. 5 (2017) 7961–7971.
[58] R.C. Che, C.Y. Zhi, C.Y. Liang, X.G. Zhou, Appl. Phys. Lett. 88 (2006), 033105.
[59] R.C. Che, L.M. Peng, X.F. Duan, Q. Chen, X.L. Liang, Adv. Mater. 16 (2004) 401–405.
[60] Z. Wu, K. Pei, L. Xing, X. Yu, W. You, R. Che, Adv. Funct. Mater. 29 (2019), 1901448.
[61] W. Yuan, J. Yang, F. Yin, Y. Li, Y. Yuan, Compos. Commun. 19 (2020) 90–98.
[62] S. Lin, S. Ju, G. Shi, J. Zhang, Y. He, D. Jiang, J. Mater. Sci. 54 (2019) 7165–7179.
[63] K. Zhou, Y. Zhao, X. Sun, Z. Yuan, G. Zheng, K. Dai, L. Mi, C. Pan, C. Liu, C. Shen, Nano Energy 70 (2020), 104546.
[64] Z. Yuan, G. Shen, C. Pan, Z.L. Wang, Nano Energy 73 (2020), 104764.
[65] Z. Huo, X. Wang, Y. Zhang, B. Wan, W. Wu, J. Xi, Z. Yang, G. Hu, X. Li, C. Pan, Nano Energy 73 (2020), 104744.
[66] Q. Hua, J. Sun, H. Liu, X. Cui, K. Ji, W. Guo, C. Pan, W. Hu, Z.L. Wang, Nano Energy 78 (2020), 105312.
[67] K. Xia, W. Wu, M. Zhu, X. Shen, Z. Yin, H. Wang, S. Li, M. Zhang, H. Wang, H. Lu, A. Pan, C. Pan, Y. Zhang, Sci. Bull. 65 (2020) 343–349.

Ruiqi Zhu received her B.S. degree from Wuhan University of Technology in 2019. Currently she is pursuing her M.S. degree under the supervision of Prof. Ronghai Yu and Prof. Xiaofang Liu at Beihang University. Her current research interests focus on electromagnetic functional materials and devices.

Zhenyang Li received his M.S. degree from Shandong University in 2019. Currently he is pursuing his Ph.D. degree under the supervision of Prof. Ronghai Yu and Prof. Xiaofang Liu at Beihang University. His current research interests focus on electromagnetic functional materials and hydrogenstorage materials.

Deng Gao received his B.S. degree from Wuhan University of Technology in 2018. Now he is pursuing his Ph.D. degree under the supervision of Prof. Ronghai Yu and Prof. Xiaofang Liu at Beihang University. His research interests focus on electromagnetic functional materials and devices.

Yuanhang Yu received her B.S. degree from University of Southwest Jiaotong in 2019. Currently she is pursuing her M.S. degree under the supervision of Prof. Xiaofang Liu at Beihang University. Her current research interests focus on electromagnetic functional materials.

Jianglan Shui is a professor of School of Materials Science and Engineering, Beihang University. He received his first Ph.D. degree from University of Science and Technology of China in 2006, and his second Ph.D. degree from University of Rochester in 2010. From 2010–2014, Shui worked as a postdoctor at Agnone National Laboratory and Case Western Reserve University. His research focuses on electrocatalysts, PEM fuel cell and hydrogen storage materials.

Ronghai Yu is a professor of School of Materials Science and Engineering, Beihang University. He received his Ph.D. degree in Physics from the University of Barcelona, Spain in 1995. He was a professor in the Department of Materials Science and Engineering, Tsinghua University from 2003 to 2009. His research interests focuses on magnetic functional materials and hydrogen storage materials.

Dr. Caofeng Pan received his B.S. degree (2005) and his Ph.D. (2010) in Materials Science and Engineering from Tsinghua University, China. He then joined the Georgia Institute of Technology as a postdoctoral fellow. He is currently a professor and a group leader at Beijing Institute of Nanoenergy and Nanosystems, Chinese Academy of Sciences since 2013. His main research interests focus on the fields of piezotronics/piezo-phototronics for fabricating new electronic and optoelectronic devices, nano-power source (such as nanofuel cell, nano biofuel cell and nanogenerator), hybrid nanogenerators, and self-powered nanosystems. Details can be found at http://www.piezotronics.cn.

Xiaofang Liu is an associate professor of School of Materials Science and Engineering, Beihang University. She received her Ph.D. degree in Materials Science and Engineering from Tsinghua University in 2010. In the period from 2013 to 2014, she collaborated with Prof. Yadong Yin as a visiting scholar at University of California, Riverside. Her research interests focuses on magnetic functional materials/devices and hydrogen storage materials.